Supporting Information

Supporting Information Corrected June 25, 2018

Rashidian et al. 10.1073/pnas.1502609112

SI Materials and Methods

Synthesis of $(Gly)_3$-Texas Red.

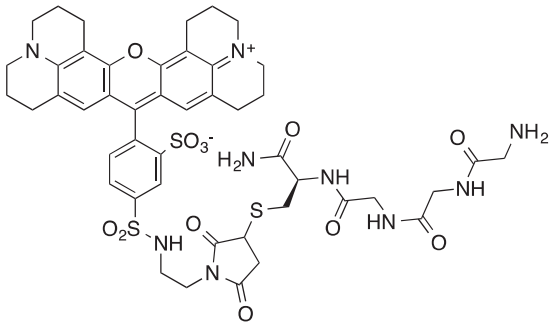

The tetrapeptide GGGC was synthesized by standard solid-phase peptide synthesis. Maleimide-Texas Red (Vector Laboratories) was dissolved in 20 mM $NaHCO_3$ buffer (pH 8.3). The tetrapeptide GGGC was added and left to stir at room temperature for 3 h until TLC (1:2 Hex:EtOAc vol/vol) indicated near-complete conversion to the product. The solution was filtered and purified by reverse-phase HPLC with a semipreparative column (C_{18} column, Gemini, 5 μm, 10 × 250 mm; Phenomenex) at a flow rate of 5.0 mL/min: solvent A, 0.1% TFA in H_2O; solvent B, 0.1% TFA in CH_3CN. $(G)_3$-Texas Red eluted at 40–45% (vol/vol) solvent B. Fractions containing pure product were collected and lyophilized. LC-MS calculated for $C_{46}H_{54}N_9O_{12}S_3[M+H]^+$ was 1,020.305, found 1,020.310.

Mice. All animals used for FACS and two-photon experiments were housed at the Whitehead Institute for Biomedical Research, and maintained under specific pathogen-free conditions. The experiments were performed in accordance with institutional, state, and federal guidelines. C57BL/6, NOD/SCID, CD11b-deficient, and MHC-II–deficient mice were purchased from Jackson Laboratories. MHC II–eGFP mice have been described previously (15).

Two-Photon Imaging. Two-photon imaging was performed with an Olympus BX61 upright microscope (Olympus 25× 1.05 NA Plan Objective), fitted with a SpectraPysics MaiTai DeepSee laser. Images were acquired using 910-nm excitation and the following filters: second-harmonic emission (Collagen) (460–510 nm) and GFP (495–540 nm), separated by a 505-nm dichroic mirror, and a third filter (575–630 nm) for the Texas Red signal. Images were acquired with 5-μm Z resolution with Olympus FluoView FC1000 software. Tile images (Fig. 3*H*) were saved as JPEG files. Images in Fig. 2 *F* and *G* were processed to obtain a scale bar in Imaris, version 7.4.0; no intensity or contrast adjustments were made.

Synthesis of ^{18}F-TCO. The 2-[^{18}F]-(*E*)-5-(2-Fluoroethoxy)cyclooct-1-ene (^{18}F-TCO) was prepared as described (1). [^{18}F]-Fluoride [no carrier added (n.c.a.)] in $H_2{}^{18}O$, purchased from PETNET, was transferred to a microwave reaction vessel (10 mL) and diluted with Kryptofix 2.2.2 (33 mM in 300 μL of MeCN) and K_2CO_3 (33 mM in 300 μL of H_2O) solutions. The [^{18}F]-F/K222/K_2CO_3 solution, 87.3 ± 22.6 mCi (3,230.1 ± 836.2 MBq), was dried by azeotropic distillation of water with MeCN (added at 2, 6, and 8 min) by microwave heating (98 °C, 150 W, 15 min) under a stream of argon. After drying, (*E*)-2-(cyclooct-4-enyloxy) ethyl 4-methylbenzenesulfonate (4 mg, 30 mmol) in DMSO was added, the vessel was sealed, and the reaction was heated by microwave (75 W) to 90 °C for 10 min. After cooling to 50 °C, the mixture was diluted with MeCN (150 μL) and H_2O (750 μL) and subjected to preparative HPLC purification (1:1 MeCN/H_2O, 0.1% formic acid at 5.5 mL/min using a Macherey-Nagel Nucleodur C18 Pyramid 10 × 250 mm Vario-Prep column). ^{18}F-TCO was collected (t_R = 13.5 min) in 5–6 mL of solvent, diluted with H2O (40 mL), and isolated by manual C18 solidphase extraction. Elution from the C18 cartridge with DMSO (4 × 200 μL) gave 22.1 ± 4.0 mCi (817.6 ± 149.5 MBq), a 35.6 ± 4.9% decay-corrected radiochemical yield.

PET-CT Imaging. For all imaging experiments, mice were anesthetized using 1.5% isoflurane in O_2 at a flow rate of ∼1 L/min. Mice were imaged with PET-computed tomography (CT) using an Inveon small-animal scanner (Siemens). Each PET acquisition took ∼30 min. High-resolution Fourier rebinned PET images were reconstructed by a 3D ordered subsets expectation algorithm using maximum a priori (OSEM3D/MAP) with 18 MAP iterations and 2 OSEM3D iterations into 0.796 × 0.796 × 0.861 mm images on a 128 × 128 × 159 image matrix. Peak sensitivity of the Inveon accounts for 11.1% of positron emission, with a mean resolution of 1.65 mm. More than 100 counts were acquired per pixel, and the mean signal-to-noise ratio was greater than 20. CT images were acquired using an 80 kVp 500 mA X-ray tube over 360 projections on a 125-mm detector. A modified Feldkamp conebeam reconstruction algorithm (COBRA; Exxim) was used to reconstruct the CT images into a 110-μm isotropic image matrix of 512 × 512 × 768. Reconstruction of datasets, PET-CT registration, and image analysis were performed using IRW software (Siemens). Two-dimensional and 3D visualizations were produced using the DICOM viewer OsiriX (OsiriX Foundation).

Blood Half-Life Measurement of ^{18}F-VHHs. Mice were administered 30 ± 3 μCi of ^{18}F-VHH7 by i.v. tail-vein injection. Blood samples were obtained by retroorbital puncture using tared, heparinized capillary tubes. Blood samples and capillaries were weighed, and radioactivity was measured using a Perkin-Elmer Wallac Wizard 3″ 1480 Automatic Gamma Counter. Values, expressed as percentages of the injected dose per gram of tissue, were fit (least squares) to a two-compartment biexponential decay model performed using GraphPad Prism 4.0c (Fig. S2).

Biodistribution Analysis of ^{18}F- or ^{64}Cu-VHHs. Mice were administered 296 ± 19 μCi of labeled VHHs by i.v. tail-vein injection. At 2 h postinjection, mice were euthanized, perfused with 1× PBS (20 mL), and dissected. Blood, urine, and tissues were excised, and their wet weight was determined. Tissue radioactivity was measured with a Perkin-Elmer Wallac Wizard 3″ 1480 Automatic Gamma Counter. Statistical analysis was performed using GraphPad Prism 4.0c. Values are expressed as percentages of the injected dose (excretion subtracted) per gram of tissue.

PET Standard Uptake Value Calculation. Standard uptake value (SUV) is the derived ratio of tissue radioactivity concentration (Bq/mL) and the injected radioactivity per gram of the mouse's body weight. The calculation used the following equation: SUV = (region of interest radioactivity concentration)/(injected activity/mouse total mass).

Analysis of the Purity of the Radiolabeled VHHs. The purity of the radiolabeled VHHs was assessed with TLC performed on silica-impregnated glass sheets (ITLC plates; Pall Life Sciences). Plates for ^{18}F-VHHs were developed with 100% acetonitrile whereas ^{64}Cu-VHH plates were developed using 50 mM EDTA (pH 7.0) and analyzed using a Bioscan AR-2000 scanner operated by the WinScan V3 software package (Fig. S5).

Generation and Sequence Identity of VHH7 and VHHDC13. Two VHHs, VHH7 (anti-class II MHC) and VHHDC13 (anti-CD11b) were generated following standard procedures (2).

VHH7. QVQLQESGGG LVQAGDSLRL SCAASGRTFS RGVMGWFRRA PGKEREFVAI FSGSSWSGRS TYYSDSVKGR FTISRDNAKN TVYLQMNGLK PEDTAVYYCA AGYPEAYSAY GRESTYDYWG QGTQVTVSS GGLPETG GHHHHHH

VHHDC13. QVQLQESGGG LVQAGGSHNL SCTASGITFS SLAMGWFRQT PGKEREFVAN IMRSGSSVFY ADSVRGRFTI SRDNAKNTAH LQMNSLKPED TAVYFCAATR GAWPAEYWGQ GTQVTVSS GGLPETG GHHHHHH

1. Keliher EJ, Reiner T, Turetsky A, Hilderbrand SA, Weissleder R (2011) High-yielding, two-step 18F labeling strategy for 18F-PARP1 inhibitors. *ChemMedChem* 6(3):424–427.

2. Pardon E, et al. (2014) A general protocol for the generation of Nanobodies for structural biology. *Nat Protoc* 9(3):674–693.

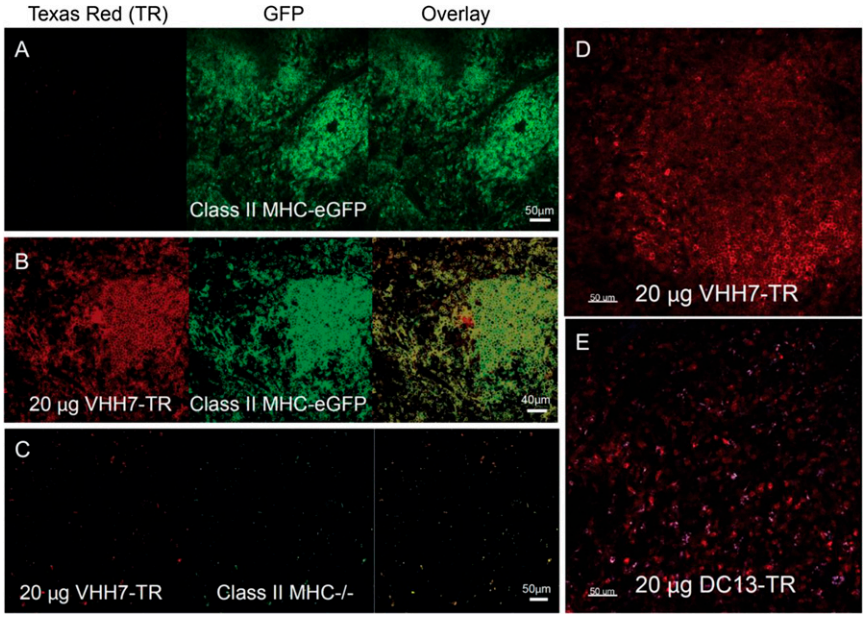

Fig. S1. VHH7 (anti-mouse class II MHC) and VHHDC13 (anti-mouse CD11b) stain spleen. VHHs were site-specifically labeled with Texas Red via sortagging. Images were acquired using two-photon microscopy. In *A*–*C*, the *Left* and *Middle* panels show the Texas Red and GFP channels, respectively. The *Right* panels are overlays. (*A*) Images of a spleen of an MHC-II–eGFP knock-in mouse, with no VHH injection before imaging. (*B*) Images of a spleen of an MHC-II–eGFP knock-in mouse injected with 20 μg of VHH7-Texas Red 90 min before imaging. (*C*) Images of a spleen of an MHC-II$^{-/-}$ mouse injected with 20 μg of VHH7-Texas Red 90 min before imaging. (*D*) Image of a spleen of a B6 mouse injected with 20 μg of VHH7-Texas Red 90 min before imaging. (*E*) Image of a spleen of a B6 mouse injected with 20 μg of VHHDC13-Texas Red 90 min before imaging. All injections were done intravenously.

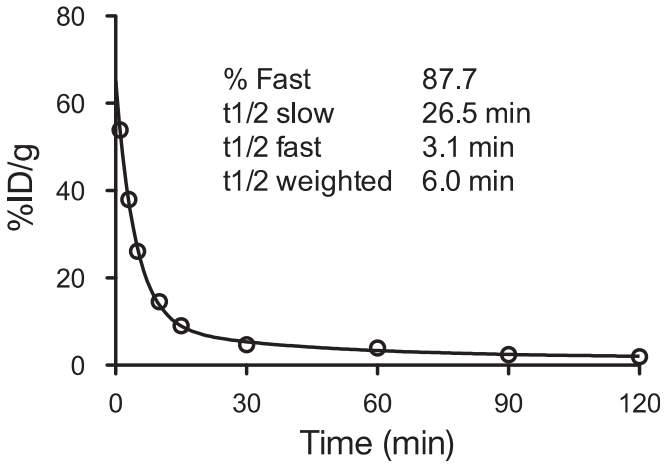

Fig. S2. Blood half-life data for ^{18}F-VHH7. Data are reported as percentage of injected dose per gram of blood (%ID/g). Data were fit to a two-compartment model (biexponential nonlinear regression) to give a weighted blood half-life of 6.0 min.

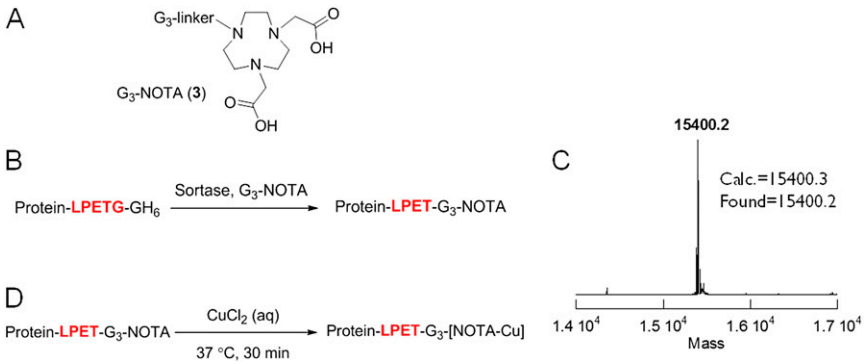

Fig. S3. Schematic representation of sortase-mediated site-specific labeling of VHHs with ^{64}Cu. (*A*) Structure of sortase substrate, $(Gly)_3$-NOTA. (*B*) A VHH equipped with a sortase recognition motif was modified with $(Gly)_3$-NOTA substrate using a sortase reaction and confirmed by LC-MS (Cu-NOTA–VHH7 shown in *C*). (*D*) NOTA-labeled VHH was incubated with ^{64}Cu solution to provide radiolabeled protein.

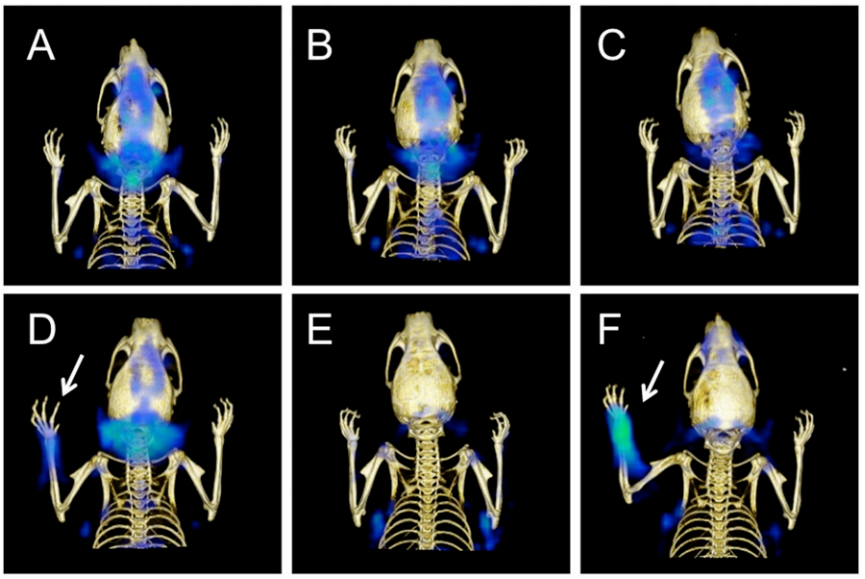

Fig. S4. ^{64}Cu-VHH7 (anti-mouse class II MHC) and ^{64}Cu-VHHDC13 (myeloid cell-specific) detect secondary lymphoid organs and inflammation. (*A*–*C*) PET images of C57BL/6 mouse 4 h, 8 h, and 24 h postinjection of ^{18}F-VHH7, respectively, demonstrating specificity for class II MHC organs. (*E*) PET image of C57BL/6 mouse 4 h postinjection of ^{18}F-VHHDC13, demonstrating specificity for myeloid cells. (*D* and *F*) Complete Freund's adjuvant (CFA) was injected to the left paw of C57BL/6 mice, and ^{64}Cu-VHH7 (*D*) or ^{64}Cu-VHHDC13 (*F*) was used to image inflammation 24 h after CFA injection. Images were obtained 4 h postinjection of ^{64}Cu-VHHs; inflammation around the injection site is clearly visible, attributable to influx of host-derived class II^+ or myeloid cells for *D* and *F*, respectively (arrows). Images are all window-leveled to the same intensity for better comparison.

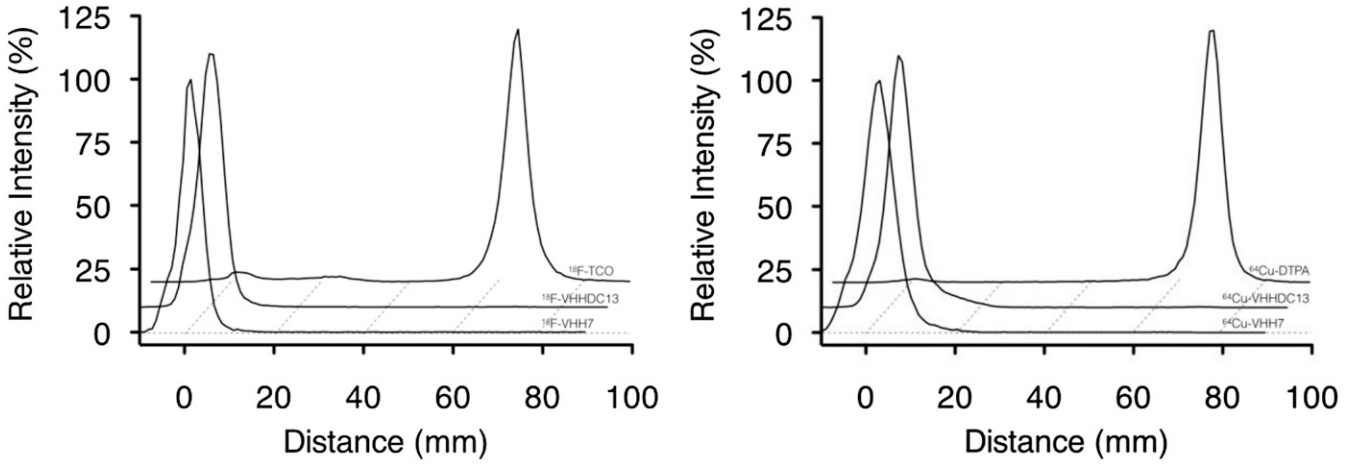

Fig. S5. Radio-TLC analysis of ^{18}F- and ^{64}Cu-VHHs. Radio-TLC analysis of labeled VHHs was performed after size-exclusion chromatography demonstrating >98% radiochemical purity of all labeled VHHs.

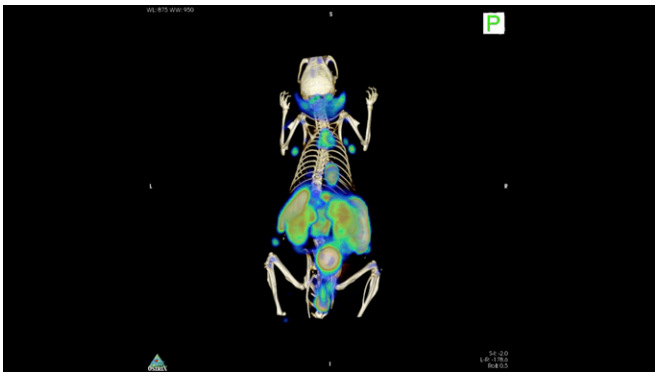

Movie S1*A*. ^{18}F-VHH7 (anti-mouse class II MHC) detects secondary lymphoid organs. PET-CT movie of a C57BL/6 mouse, 2 h postinjection of ^{18}F-VHH7. Movies and images are representative of two to four mice with similar results.

Movie S1*A*

Movie S1*B*. ^{18}F-VHH7 (anti-mouse class II MHC) detects secondary lymphoid organs. PET-CT movie of a C57BL/6 mouse, 2 h postinjection of ^{18}F-VHH7. Movies and images are representative of two to four mice with similar results.

Movie S1*B*

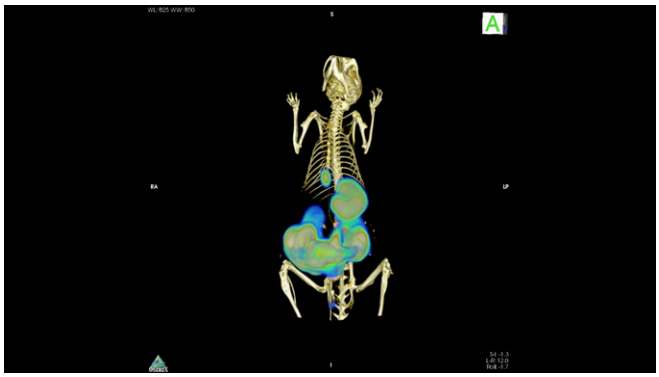

Movie S2*A*. PET-CT movie of a class II MHC$^{-/-}$ mouse, 2 h postinjection of ^{18}F-VHH7. Movies and images are representative of two to four mice with similar results.

Movie S2*A*

Movie S2*B*. PET-CT movie of a class II MHC$^{-/-}$ mouse, 2 h postinjection of ^{18}F-VHH7. Movies and images are representative of two to four mice with similar results.

Movie S2*B*

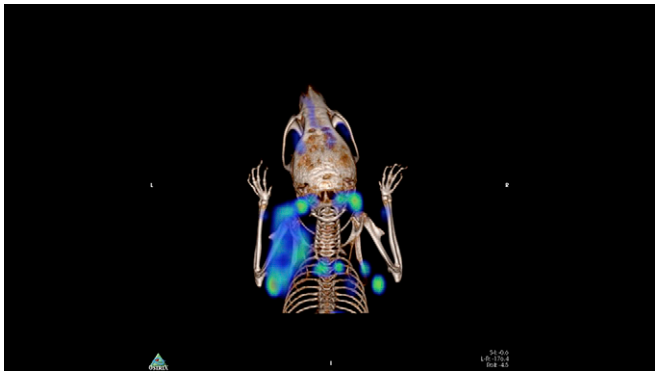

Movie S3. Imaging the presence of tumor-associated class II MHC^{+} cells using ^{18}F-VHH7 (anti-mouse class II MHC). A NOD-SCID mouse was inoculated s.c. on the left shoulder with human Mel-Juso melanoma cells and imaged 35 d postinjection. Tumor cells lack mouse class II MHC molecules. Clearly, different sets of bilaterally symmetrically disposed lymph nodes and tumor-associated class II MHC-positive cells are visible, attributable to influx of host-derived class II MHC-positive cells. Note the enlarged tumor-draining lymph node in comparison with the nondraining LN. Movies and images are representative of two to four mice with similar results.

Movie S3

Movie S4. Imaging the presence of tumor-associated CD11b^{+} cells using ^{18}F-VHHDC13 (anti-mouse CD11b). A NOD-SCID mouse was inoculated s.c. on the left shoulder with human Mel-Juso melanoma cells and imaged 35 d postinjection. Tumor cells lack mouse CD11b molecules. Clearly the tumor-associated CD11b-positive cells are visible, attributable to influx of host-derived CD11b-positive cells. Movies and images are representative of two to four mice with similar results.

Movie S4

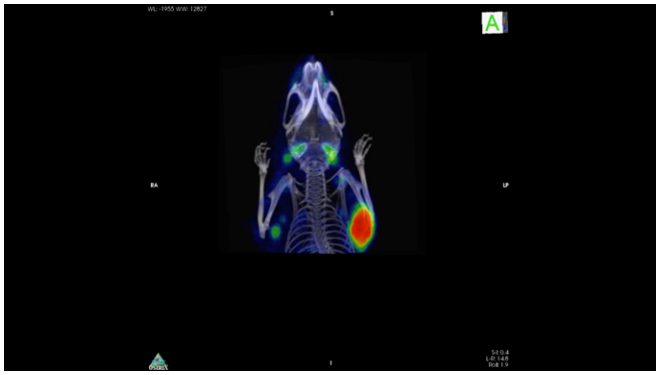

Movie S5*A*. Imaging the presence of tumor-associated CD11b^{+} cells using ^{18}F-VHHDC13 (anti-mouse CD11b). A WT mouse was inoculated s.c. on the left shoulder with mouse B16 melanoma cells and imaged 7 d postinjection. Tumor cells lack mouse CD11b molecules. Clearly the tumor-associated CD11b-positive cells are visible, attributable to influx of host-derived CD11b-positive cells. Movies and images are representative of two to four mice with similar results.

Movie S5*A*

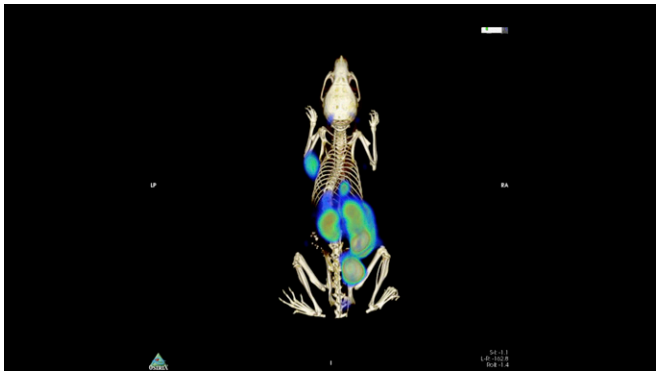

Movie S5*B*. Imaging the presence of tumor-associated CD11b^{+} cells using ^{18}F-VHHDC13 (anti-mouse CD11b). A WT mouse was inoculated s.c. on the left shoulder with mouse B16 melanoma cells and imaged 7 d postinjection. Tumor cells lack mouse CD11b molecules. Clearly the tumor-associated CD11b-positive cells are visible, attributable to influx of host-derived CD11b-positive cells. Movies and images are representative of two to four mice with similar results.

Movie S5*B*

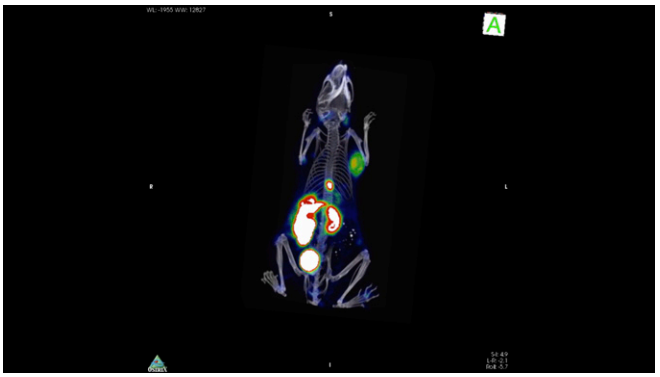

Movie S5*C*. Imaging the presence of tumor-associated CD11b^{+} cells using ^{18}F-VHHDC13 (anti-mouse CD11b). A WT mouse was inoculated s.c. on the left shoulder with mouse B16 melanoma cells and imaged 7 d postinjection. Tumor cells lack mouse CD11b molecules. Clearly the tumor-associated CD11b-positive cells are visible, attributable to influx of host-derived CD11b-positive cells. Movies and images are representative of two to four mice with similar results.

Movie S5C

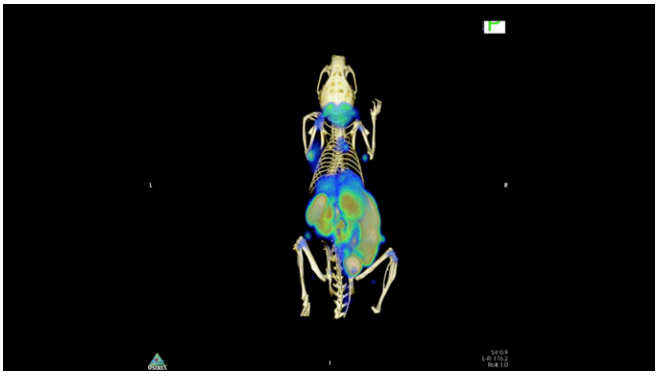

Movie S6*A*. Imaging the presence of tumor-associated class II MHC^{+} cells using ^{18}F-VHH7 (anti-mouse class II MHC). A WT mouse was inoculated s.c. on the left shoulder with mouse B16 melanoma cells and imaged 7 d postinjection. Tumor cells lack mouse class II MHC molecules. Movies and images are representative of two to four mice with similar results.

Movie S6A

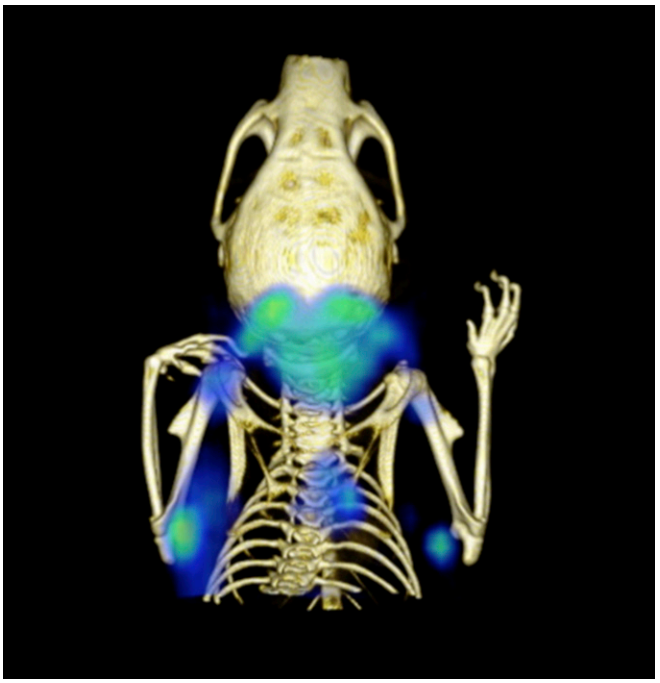

Movie S6*B*. Imaging the presence of tumor-associated class II MHC^{+} cells using ^{18}F-VHH7 (anti-mouse class II MHC). A WT mouse was inoculated s.c. on the left shoulder with mouse B16 melanoma cells and imaged 7 d postinjection. Tumor cells lack mouse class II MHC molecules. Movies and images are representative of two to four mice with similar results.

Movie S6*B*

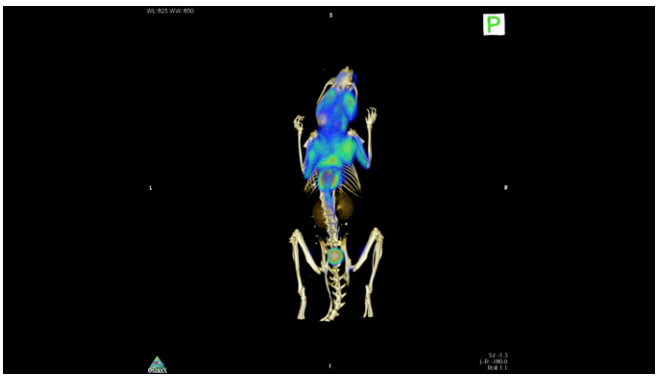

Movie S7. Imaging the presence of tumor cells using ^{18}F-FDG. A WT mouse was inoculated s.c. on the left shoulder with mouse B16 melanoma cells and imaged 7 d postinjection. Higher metabolic activity of the right shoulder's muscle relative to the left shoulder's muscle is probably due to the presence of the tumor on the left shoulder, which makes the mouse use its right shoulder more often than the left one to walk around. The tumor on the left shoulder is visible but with inferior specificity relative to VHHs. Movies and images are representative of two to four mice with similar results.

Movie S7

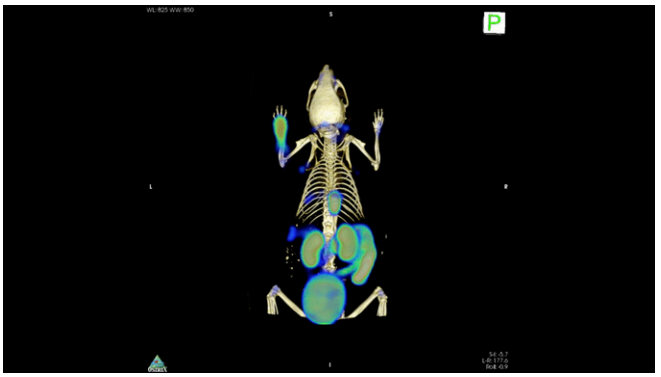

Movie S8*A*. Complete Freund's adjuvant (CFA) was injected into the left paw of C57BL/6 mice, and ^{18}F-VHHDC13 was used 24 h after CFA injection for imaging. PET-CT Images were obtained 1.5 h postinjection of ^{18}F-agent. Movies and images are representative of two to four mice with similar results.

Movie S8*A*

Movie S8*B*. Complete Freund's adjuvant (CFA) was injected into the left paw of C57BL/6 mice, and ^{18}F-VHHDC13 was used 24 h after CFA injection for imaging. PET-CT Images were obtained 1.5 h postinjection of ^{18}F-agent. Movies and images are representative of two to four mice with similar results.

Movie S8*B*

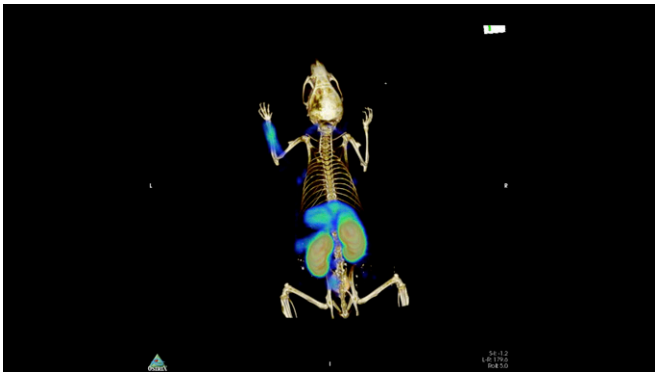

Movie S9. Complete Freund's adjuvant (CFA) was injected into the left paw of C57BL/6 mice, and ^{64}Cu-VHHDC13 was used 24 h after CFA injection for imaging. PET-CT images were obtained 4 h postinjection of ^{18}F-agent. Movies and images are representative of two to four mice with similar results.

Movie S9

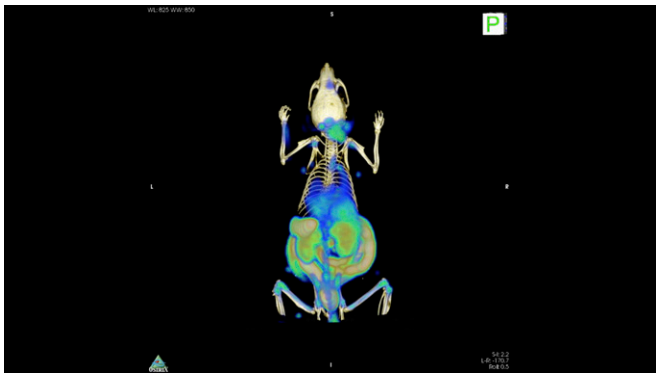

Movie S10. Complete Freund's adjuvant (CFA) was injected into the left paw of C57BL/6 mice, and ^{18}F-VHH7 was used 24 h after CFA injection for imaging. PET-CT images were obtained 1.5 h postinjection of ^{18}F-agent. Movies and images are representative of two to four mice with similar results.

Movie S10

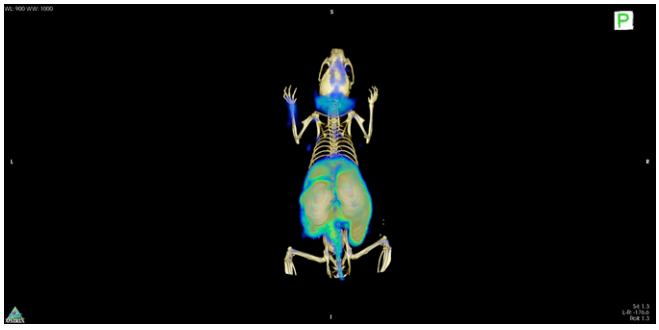

Movie S11. Complete Freund's adjuvant (CFA) was injected into the left paw of C57BL/6 mice, and ^{64}Cu-VHH7 was used 24 h after CFA injection for imaging. PET-CT Images were obtained 4 h postinjection of ^{64}Cu-agent. Movies and images are representative of two to four mice with similar results.

Movie S11

Movie S12*A*. Complete Freund's adjuvant (CFA) was injected into the left paw of C57BL/6 mice, and ^{18}F-FDG was used 24 h after CFA injection for imaging. PET-CT Images were obtained 1.5 h postinjection of ^{18}F-agent. Higher metabolic activity of the right shoulder's muscle relative to the left shoulder's muscle is probably due to the inflammation of the left paw, which makes the mouse use its right shoulder more than the left one to walk around. Movies and images are representative of two to four mice with similar results.

Movie S12*A*

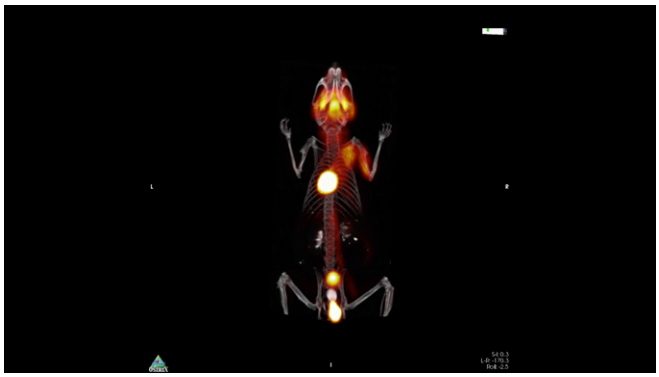

Movie S12*B*. Complete Freund's adjuvant (CFA) was injected into the left paw of C57BL/6 mice, and ^{18}F-FDG was used 24 h after CFA injection for imaging. PET-CT Images were obtained 1.5 h postinjection of ^{18}F-agent. Higher metabolic activity of the right shoulder's muscle relative to the left shoulder's muscle is probably due to the inflammation of the left paw, which makes the mouse use its right shoulder more than the left one to walk around. Movies and images are representative of two to four mice with similar results.

Movie S12*B*

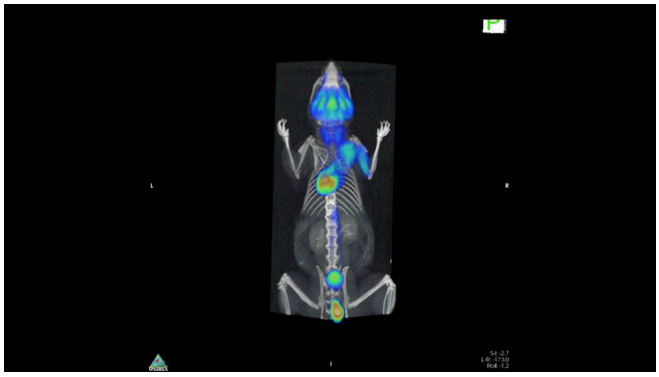

Movie S12*C*. Complete Freund's adjuvant (CFA) was injected into the left paw of C57BL/6 mice, and ^{18}F-FDG was used 24 h after CFA injection for imaging. PET-CT Images were obtained 1.5 h postinjection of ^{18}F-agent. Higher metabolic activity of the right shoulder's muscle relative to the left shoulder's muscle is probably due to the inflammation of the left paw, which makes the mouse use its right shoulder more than the left one to walk around. Movies and images are representative of two to four mice with similar results.

Movie S12*C*

Image S1. Image of a lymph node of a WT mouse, with no VHH injection before imaging. VHH7 (anti-mouse class II MHC) and VHHDC13 (anti-mouse CD11b) stain secondary lymphoid organs. VHHs were site-specifically labeled with Texas Red via sortagging. Images were acquired by two-photon microscopy. Movies and images are representative of two to four mice with similar results.

Image S1

Image S2. Image of a lymph node of a WT mouse injected with 20 μg of VHH7-Texas Red 90 min before imaging. VHH7 (anti-mouse class II MHC) and VHHDC13 (anti-mouse CD11b) stain secondary lymphoid organs. VHHs were site-specifically labeled with Texas Red via sortagging. Images were acquired by two-photon microscopy. Movies and images are representative of two to four mice with similar results.

Image S2

Image S3. Image of a lymph node of an MHC-II$^{-/-}$ mouse injected with 20 μg of VHH7-Texas Red 90 min before imaging. VHH7 (anti-mouse class II MHC) and VHHDC13 (anti-mouse CD11b) stain secondary lymphoid organs. VHHs were site-specifically labeled with Texas Red via sortagging. Images were acquired by two-photon microscopy. Movies and images are representative of two to four mice with similar results.

Image S3

Image S4. Image of a lymph node of a B6 mouse injected with 20 μg of DC13-Texas Red 90 min before imaging. VHH7 (anti-mouse class II MHC) and VHHDC13 (anti-mouse CD11b) stain secondary lymphoid organs. VHHs were site-specifically labeled with Texas Red via sortagging. Images were acquired by two-photon microscopy. Movies and images are representative of two to four mice with similar results.

Image S4